



**HAL**  
open science

# Precursors-driven machine learning prediction of chaotic extreme pulses in Kerr resonators

Saliya Coulibaly, Florent Bessin, Marcel Clerc, Arnaud Mussot

## ► To cite this version:

Saliya Coulibaly, Florent Bessin, Marcel Clerc, Arnaud Mussot. Precursors-driven machine learning prediction of chaotic extreme pulses in Kerr resonators. *Chaos, Solitons & Fractals*, 2022, 160, pp.112199. 10.1016/j.chaos.2022.112199 . hal-04505161

**HAL Id: hal-04505161**

**<https://hal.science/hal-04505161v1>**

Submitted on 22 Jul 2024

**HAL** is a multi-disciplinary open access archive for the deposit and dissemination of scientific research documents, whether they are published or not. The documents may come from teaching and research institutions in France or abroad, or from public or private research centers.

L'archive ouverte pluridisciplinaire **HAL**, est destinée au dépôt et à la diffusion de documents scientifiques de niveau recherche, publiés ou non, émanant des établissements d'enseignement et de recherche français ou étrangers, des laboratoires publics ou privés.



Distributed under a Creative Commons Attribution - NonCommercial 4.0 International License

# Precursors-driven machine learning prediction of chaotic extreme pulses in Kerr resonators

Saliya Coulibaly<sup>a,\*</sup>, Florent Bessin<sup>b</sup>, Marcel G. Clerc<sup>c</sup> and Arnaud Mussot<sup>a</sup>

<sup>a</sup>Université de Lille, CNRS, UMR 8523 - PhLAM - Physique des Lasers Atomes et Molécules, F-59000 Lille, France.,

<sup>b</sup>Aston Institute of Photonics Technologies, Aston University, Birmingham B4 7ET, UK.,

<sup>c</sup>Departamento de Física and Millennium Institute for Research in Optics, FCFM, Universidad de Chile, Casilla 487-3, Santiago, Chile.,

## ARTICLE INFO

### Keywords:

Spatiotemporal Chaos  
Kerr frequency combs  
Forecasting extreme events  
Machine Learning  
Long Short-Term Memory (LSTM)  
encoder-decoder  
Transfer Entropy

## ABSTRACT

Machine learning algorithms have opened a breach in the prediction's fortress of high-dimensional chaotic systems. Their ability to find hidden correlations in data can be exploited to perform model-free forecasting of spatiotemporal chaos and extreme events. However, the extensive feature of these evolutions makes up a critical limitation for full-size forecasting processes. Hence, the main challenge for forecasting relevant events is to establish the set of pertinent information. Here, we identify precursors from the transfer entropy of the system and a deep Long Short-Term Memory network to forecast the complex dynamics of a system evolving in a high-dimensional spatiotemporal chaotic regime. Performances of this triggerable model-free prediction protocol based on the information flowing map are tested from experimental data originating from a passive resonator operating in such a complex nonlinear regime. We have been able to predict the occurrence of extreme events up to 9 round trips after the detection of precursor, *i.e.*, 3 times the horizon provided by Lyapunov exponents, with 92% of true positive predictions leading to 60% of accuracy.

## 1. Introduction


Large-aspect-ratio deterministic systems operating out of equilibrium can become extremely sensitive to the initial conditions when undergoing chaotic spatiotemporal evolution [1–4]. Spatiotemporal chaos may be understood as the exponential destruction of information in both time and space, making the dynamics require many spatially distributed chaotic elements to be described [5]. With these elements, accurate modeling of such a system lies in two key points—a good description of the physical equations and minimal uncertainty in the initial conditions. Despite many years of intensive research to understand the complex dynamics of chaos, most are limited to theoretical investigations. Only a few experimental works had been reported due to the huge precision required to gain knowledge on the initial conditions. Recently, improvements of supervised machine learning algorithms have brought new perspectives for the forecasting of spatiotemporal complex dynamics in optics [6], economy [7], power grid load [8], and meteorology [9–11], to mention a few. These studies were performed mainly using deep learning, recurrent, and echo state networks. By providing model free processes it could be possible that chaos theory tools are no more necessary to handle time series in general. Even though powerful, the performances of machine learning-based forecasting can be compromised when dealing with spatiotemporal chaos. Indeed, the specificity of this chaos is its extensive feature. The larger the system, the larger the number of the coupled nodes in the network. This makes the problem rapidly unsolvable


for high-dimensional spatiotemporal chaotic systems. Thus, alternative strategies based on local intensive order parameters other than predicting the whole system are needed.

Here, we show that model-based and model-free tools can be combined to provide triggerable local forecasting of the extreme events in chaotic regimes. Namely, the forecasting process is activated when relevant information is identified. Answering the question of *when* and *where* the extreme events will emerge, we also address the question of *what is coming?* We will also forecast the profile of the coming event. Our strategy is depicted by the Fig. 1. First, from output signals of a resonator operating in a highly chaotic regime we identify relevant pairs. Next, they are used to train a neural network. The pre-trained network is deployed to monitor the dynamics in live and trigger the forecast when a precursor is detected. Our manuscript is organized as follows. After describing how the precursors are found in the Sec. 2, we describe the experimental setup in Sec. 3. In Sec. 4 we recall some basic of high dimensional chaos, before introducing the methods we will use to estimate the range the local dynamical regions to be forecasted Sec. 5. The details of our model-free prediction process and the results are provided in Sec. 6, followed by the concluding remarks in Sec. 7.

## 2. Complex dynamics characterization and information transfer

The degree of sensitivity to the initial conditions is formally deduced from the value of the largest Lyapunov exponent (LE). This exponent can be computed for low dimensional systems based on the mathematical model if known [12] or from the time series [13]. However, for extended systems, the main characteristics of the chaos require the knowledge of the continuous spectrum of LEs [14]. Hence,

 [saliya.coulibaly@univ-lille.fr](mailto:saliya.coulibaly@univ-lille.fr) (S. Coulibaly)

 <http://> (S. Coulibaly)

ORCID(S): 0000-0003-3943-6939 (S. Coulibaly); 0000-0001-8280-6304  
(.F. Bessin); 0000-0002-8006-0729 (.M.G. Clerc); 0000-0002-6428-9443 (.A. Mussot)

from experimental data, only the consequences of the chaos can be measured and not their analytical characteristics. Indeed, LE is also interpreted as the production rate of entropy during the evolution. Likewise, in high-dimensional chaos, correlation ranges between different locations in the system are much smaller than the actual size of the system. Consequently, according to information theory [15], mutual information between two locations  $x_1$  and  $x_2$  may exponentially vanish as the separation  $\|x_1 - x_2\| \rightarrow \infty$ . For a system composed of two signals  $x$  and  $y$  with joint probability  $p(x, y)$  the Shannon entropy [16] is  $H_1 = -\sum_{x,y} p(x, y) \log[p(x, y)]$ . If the same processes are supposed independent it comes  $H_2 = -\sum_{x,y} p(x, y) \log[p(x)p(y)]$ . The mutual information is then  $I_{XY} = H_2 - H_1 = \sum_{x,y} p(x, y) \log \left[ \frac{p(x,y)}{p(x)p(y)} \right]$ . To determine which of the two signals provides more information regarding its own past, it is useful to compute the transfer entropy

$$(TE) [17-21]: TE_{Y \rightarrow X} = \sum_{x,y} p(x_{n+1}, x_n^h, y_n^h) \log \left[ \frac{p(x_{n+1}|x_n^h, y_n^h)}{p(x_{n+1}|x_n^h)} \right]$$

with  $n$  the current iteration and  $h$  the history length. Hence, taking  $x$  and  $y$  as the measured data at different locations separated by  $\Delta t$  (slow time in Fig. 1) and lagging one over the other by  $\Delta \tau$  (fast time in Fig. 1), one can construct the map  $TE_{Y \rightarrow X}(\Delta t, \Delta \tau)$  or  $TE_{X \rightarrow Y}(\Delta t, \Delta \tau)$  as sketched in Fig. 1. With the two-point correlation length (see Sec. 5.2), TE will be the model-free tool that we will use to measure the impact of the spatiotemporal chaos in our system. In practice, there are a many codes that allow to compute the transfer entropy of continuous time series. Here, for our transfer entropy maps, we have used the open source JIDT software package[22] (<https://github.com/jlizer/jidt/>). The portability of this JIDT Java-based code, with no installation requirement have motivated our choice.

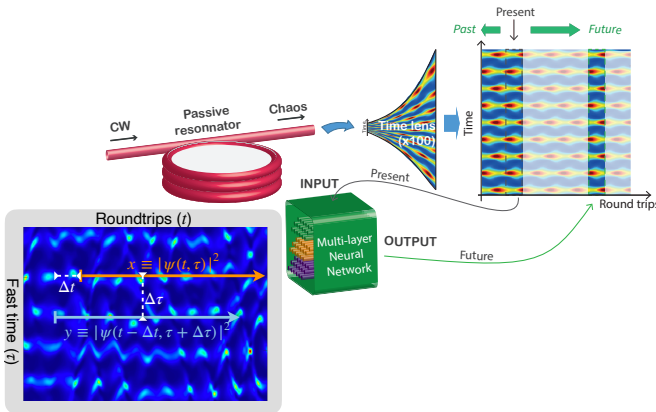


**Figure 1:** Schematic representation of prediction method of the spatiotemporal chaos at the output of the optical fiber ring synchronously pump close to a resonance frequency. CW: continuous wave. In the grey panel, we illustrate how the signals are selected to compute the transfer entropy map. The details of the multi-layer Network are given in the Appendix D section.

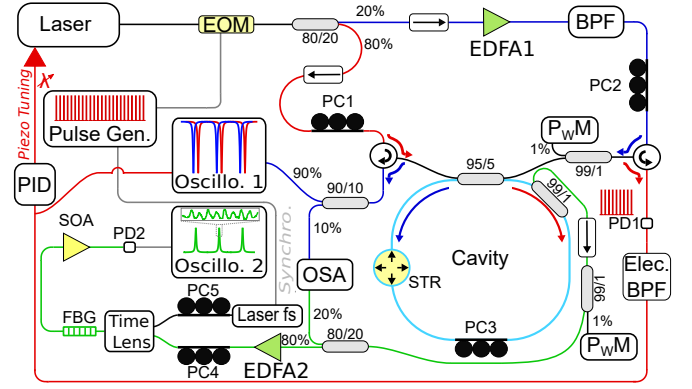


**Figure 2:** Experimental setup. P<sub>w</sub>M, powermeter; PC<sub>1-5</sub>, polarization controller; PD<sub>1-2</sub>, photodetector; OSA, optical spectrum analyzer; Elec. BPF: electronic band-pass filter; Oscillo.<sub>1-2</sub>, oscilloscope; Pulse Gen., pulse generator; EOM, electro-optic modulator; PID, proportional-integrate-derivative; EDFA<sub>1-2</sub>, erbium-doped fiber amplifier; BPF, band-pass filter; STR, fiber stretcher; FBG, fiber Bragg grating; SOA, semiconductor optical amplifier; Laser fs, femtosecond laser.

### 3. The experimental setup

A details sketch of the experimental setup is depicted in Fig. 2. It is similar to the one used in Ref. [23]. It consists of a passive fiber ring cavity built with a specially designed dispersion shifted fiber ( $\beta_{DSF} = -3.8 \text{ ps}^2/\text{km}$  at 1545 nm and  $\gamma_{DSF} = 2.5 \text{ W}^{-1}.\text{km}^{-1}$ ) closed by a 95/5 coupler made of the same fiber to get a perfectly uniform cavity of 132.9 meter-long with a finesse of 15.6. We drive the cavity with a train of square shaped pulses of 1 ns duration. This configuration prevents from stimulated Brillouin scattering and to generate high peak power to trigger the parametric process. These pulses are generated from a continuous wave (cw) laser at 1545 nm (with a narrow linewidth, less than 100 Hz) whose intensity is chopped by an electro-optic modulator (EOM). The repetition rate of these pulses is set to match with the repetition rate of the cavity, in order to drive the system synchronously and get one pulse per roundtrip. Pulses are then amplified by an erbium doped amplifier and filtered out by a thin bandwidth filter (BPF, 100 GHz) to remove amplified spontaneous emission (ASE) in excess. Finally, pump pulses are launched into the cavity through the right port of the cavity propagating in the anticlockwise direction (blue arrows). Note that, we added a 99/1 tap coupler just before the input port of the cavity for input power monitoring and setting. Due to the interferometric nature of such a system the linear phase accumulated by pump is extremely sensitive to external perturbations (change in pressure, temperature) and need to be stabilized. For this purpose, a fraction of the output power of the EOM is launched through the left port of the cavity, propagating in the clockwise direction (red arrows). This weak signal detected at the cavity output by a photodetector (PD1) provides an error signal for a feedback loop system

(proportional-integrate-derivative) which finely tunes the cw laser wavelength. As in Ref. [23, 24], a combination of three polarization controllers and measurements of a fraction of cavity output signals are used to control the cavity detuning (normalized detuning set to  $\Delta = 1.1$ , monostable [25]). In order to study the intracavity field, we added just before the coupler closing the cavity a 99/1 tap coupler. A part of this extracted field (20%) is analyzed by means of optical spectrum analyzer while the other part (80%) is amplified by a low noise EDFA and then studied by a commercial time-lens (Picoluz ultra-fast temporal magnifier, Thorlabs) based on the results published in Ref. [26].

The time stretching effect was obtained by pumping the time-lens with a femtosecond laser centered at 1570 nm providing pulses with a fixed repetition rate of 99.88 MHz. This laser was used as a reference clock for the EOM such as the repetition rate of cavity pump pulses is an exact multiple of the femtosecond laser (typically 65 times in our case). In order to drive the cavity in a perfectly coherent way, we added a stretcher inside the system, thus we could finely tune the cavity length such as the pump pulses repetition rate matched with the cavity repetition rate. The magnified signal (magnified factor of 57) was filtered by means of a fiber Bragg grating to perfectly remove the femtosecond pump in excess, and then slightly amplified by a semiconductor optical amplifier to be recorded by a fast photodiode and an oscilloscope (70 GHz bandwidth each). Thanks to this time-lens, we were able to record at each round-trip the intracavity temporal pattern over a window of 36 ps with a resolution of about 300 fs (shorter than the local dynamics time scale). We will use these data either to train the network or to test its performances.

#### 4. Spatiotemporal chaos in an optical fiber ring resonator

Figure 1 sketches up the prediction protocol of chaotic extreme pulses in a Kerr resonator. The data are obtained from a passive resonator made of an optical fiber ring synchronously pumped close to a cavity resonance. The repetition rate of the cavity is about 1.54 MHz (64.9  $\mu$ s) and the local dynamics time scale is of the order of the ps. For simplicity, the ring was set to operate in a monostable regime, *i.e.*, a region where the transmission function is single valued for a given pump power. By pumping the cavity well above the cavity threshold, typically a few times, the continuous wave solution breaks into a periodic wave train, which in turn experiences an oscillatory instability and then evolves onto a chaotic regime [27, 28]. This current sequence is universal and can be observed in many other fields of physics [5, 12]. The dynamics of the light circulating in the cavity is accurately modelled by the driven and damped nonlinear Schrödinger equation [29] (see Appendix A), referred to as Lugiato-Lefever equation (LLE) [30]. The LLE has the advantage that we can use both model-based and model-free tools to compute all the quantities needed to characterize the spatiotemporal complexity.

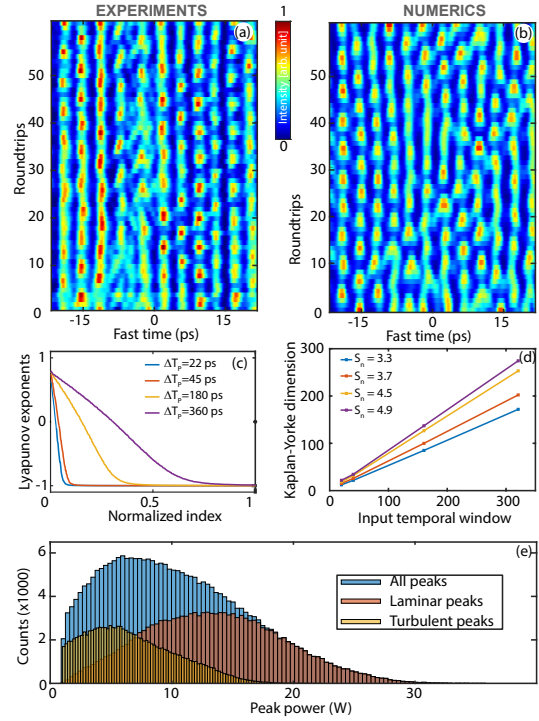


**Figure 3:** Typical spatiotemporal turbulent dynamics (a) from experiments and (b) from numerics (LLE, Eq. (S7) in supplemental documents). (c) Lyapunov spectrum for different time windows ( $\Delta T_p$ ). (d) Kaplan-Yorke dimension as function of the temporal window ( $\Delta T_p$ ) for different output power normalized to the cavity threshold ( $S_n$ ). All parameters are listed in Appendix A. (e) Probability density functions of the all the peaks (blue), laminar peaks (orange) and turbulent peaks (yellow) from numerics for a detection threshold set at the mean value of the intracavity power. The evolution of these distributions is provided as an additional material (moviepdf.gif).

Figure 3(a) shows an example of the complex behavior obtained experimentally by pumping the cavity well above the nonlinear threshold (3 times the emission threshold). It illustrates the output cavity field in the time domain, round trip to round trips. An almost periodic pulse train of 3.8 ps period with a pulse duration of typically 1.8 ps can be observed. Pulse positions and shapes modifications in this two dimensional map is characteristic of a spatiotemporal chaos [27]. We performed numerical simulations with the experimental parameters. They are depicted in Fig. 3(b). Numerical results look similar to experimental results in Fig. 3(a). The fine characterization of the complexity of this spatiotemporal chaotic regime had been performed from standard analysis tools [12] either by changing the time window or the pump power. For the sake of simplicity, since the agreement between experiments and numerics is very good, we used numerical simulations to perform these investigations. Firstly, Fig. 3(c) shows the Lyapunov spectrum evolution for different time window durations ( $\Delta T_p$ ) for a pump power set to  $S_n = 4.9$  (about 5 times the nonlinear threshold). The spectrum broadens by increasing

the time window, which is a clear signature of a spatiotemporal chaos. Secondly, Fig. 3(d) represents Kaplan-Yorke dimension evolution as a function of the temporal window for several pump powers ranging from 3.3 to 4.9 times the cavity threshold. The curves' slopes increase with the pump power that confirms the spatiotemporal chaotic nature of the process. More precisely, these slopes provide an estimation of the duration  $\Delta T_{stc}$  of independent chaotic subdomains. It is of the order of 1 ps in this case and much smaller ( $\Delta T_{stc} \ll \Delta T_p$ ) than the time window duration (36 ps here, see Figs. 3(a) and (b)). Lyapunov spectra also enable us to estimate the production rate of information during evolution along the slow time (cf. Fig. 1). For high-dimensional chaos the mean metric entropy corresponds to the Kolmogorov-Sinai entropy  $h_{KS} = \sum_{\lambda_i > 0} \lambda_i$  [31, 32]. The fluctuations lifetime over the cavity roundtrips is given by  $\tau_{stc} = 1/h_{KS}$ . From experimental parameters we found that  $\tau_{stc} < t_R$  where  $t_R$  represents the cavity roundtrip, which is a key feature of a system evolving into a high dimensional chaotic regime. On the other hand, the description of the spatiotemporal chaos can be achieved by analogy with hydrodynamics [27]. The dynamics is an irregular succession of laminar and turbulent flows. A detailed statistical study of the laminar or turbulent domains was performed in [27]. The probability distribution of the laminar/turbulent domains has the following mixture function:  $P(x) = (Ax^{-\mu} + B)e^{-mx}$ . All the constants depend only on the parameters except  $m$  which also changes with the value of the power set to separate the laminar and turbulent domains. The burst detected during the evolution can be labelled according to their location in a laminar or a turbulent flow, respectively. Distributions of all the bursts, those located in laminar, and turbulent domains are shown in Figs. 3(e) for a threshold set at the mean value the intracavity power. Highest bursts are mainly located in the laminar flows, and it is even more pronounced for highest threshold values (see movie in supplemental material for other thresholds). Hence, we can use the transfer entropy to map the information flow from the neighborhood and the past. To this end, we compute  $TE_{Y \rightarrow X}(\Delta t, \Delta \tau)$  with  $X \equiv |\psi(t, \tau)|^2$  and  $Y \equiv |\psi(t - \Delta t, \tau + \Delta \tau)|^2$ ,  $\psi$  being the considered field.

## 5. Estimation of the local dynamics range and predictability

The qualitative feature of a high dimensional complex behavior is the finite nature of the interaction range. Theory of dynamical systems and information theory have provided various estimations of this range. In a spatiotemporal chaotic regime, the equal time two-points correlation range and the Lyapunov dimension can be useful estimators.

### 5.1. Spatiotemporal chaos dimension $\xi_\delta$

The Kaplan-Yorke dimension grows linearly with the volume of a high dimensional chaotic system. For a fixed set of parameters, it is worth to provide an intensive characterization of the chaoticity level. This can be done by

computing the slope of the Kaplan-Yorke dimension curve with respect to the volume [27]. The inverse of this slope estimates the size of the independent sub-domains produced by the presence of the attractor. Figure 4(a) shows the typical evolution of  $\xi_\delta$  with respect of the pump power in the LLE. It can be seen that the range of independent sub-domains decreases with the pumping level. In the fully developed turbulent regime ( $S_n/S_{th} > 9$ ) we have  $\xi_\delta \ll \Delta T_p$ .

### 5.2. Equal time correlation dimension $\xi_2$

In the complex evolution the probability of two locations separated by  $\delta T$  to behave coherently is obtained by computing the function: [33–35]:

$$C(\delta T) = \langle (\psi(\delta T + T', t) - \langle \psi \rangle) (\psi(T', t) - \langle \psi \rangle) \rangle. \quad (1)$$

The brackets  $\langle \cdot \rangle$  stand for the average process.  $C(\delta T)$  is the equal time two-points correlation function. The computation cost of this function is generally reduced by using Wiener-Khintchin theorem [36, 37]. The correlation length  $\xi_2$  is defined as the exponential decay of  $C(\delta T)$ . For the set of parameters used here, the correlation function is shown in Fig. 4(b). We found  $\xi_2 \simeq 4.2$  ps, which is much larger than  $\xi_\delta = 1.3$  ps.

The direct determination of  $C(\Delta \tau)$  is quite costly in calculation time. However, by using the Wiener-Khintchin theorem [36, 37], it is computed by the following process: first time-averaging the Fourier spectra and next taking the inverse Fourier transform of its magnitude squared. Since the experimental spectra result from an averaging process over a large number of cavity roundtrip,  $C(\Delta \tau)$  can also be computed taking the inverse Fourier transform of the measured spectrum. Hence, for the LL equation (1), we have computed  $\xi_\delta$  and  $\xi_2$  with respect to the input pump intensity.

### 5.3. The mutual information vanishing range $\xi_I$

Finite correlation range implies a vanishing range. The information content is shared by two locations separated by  $\delta T$ . Transfer entropy is set to determine the causality in the mutual information, it can be also use to estimate  $\xi_I$ . Setting the roundtrip lag at the location of P1<sub>1</sub> the profile of the transfer entropy is shown in Fig. 4(c). It can also be seen that this quantity decays exponentially when the separation increases. We found that  $\xi_I = 4.3$  ps, which is of same order of  $\xi_2$ . The three ranges clearly suggest that the correlations in the system span beyond the chaotic subdomains. To understand the meaning of these quantities, we have represented the mean profile of the bursts in the unit of  $\xi_\delta$  and  $\xi_2 = \xi_I$  in Fig. 5. As it can be seen from this figure  $\xi_\delta$  appears to be the maximal extension of the local chaotic objects that are the burst and  $\xi_2 = \xi_I$  the range above which their information content vanishes. This sets  $\xi_2 = \xi_I$  as the best choice for the local dynamics range.

Note that the assumption of exponential decay is based on the observation in many chaotic systems. However, in such a profile, it is also expected that data follow a power

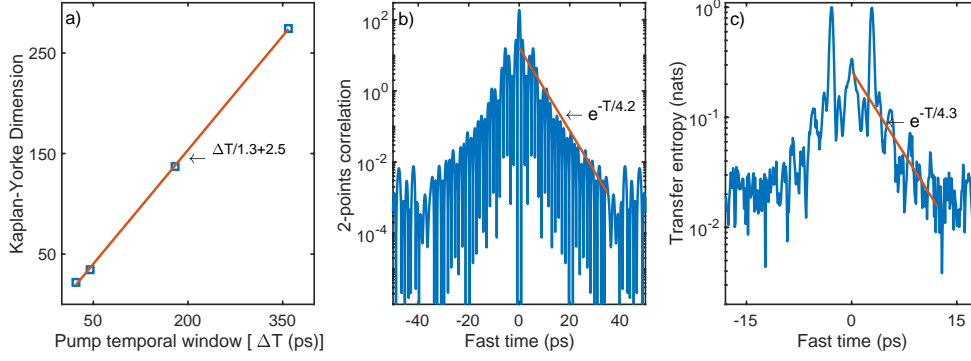


**Figure 4:** Local dynamics range of the LLE equation for  $\Delta = 1.1$  and  $S = 4.9$ . (a) Lyapunov dimension density, (b) Correspond to the equal time two-points correlation and, (c) the transfer entropy vanishing range. Red lines in (b) and (c) are the linear trend extracted from the data.

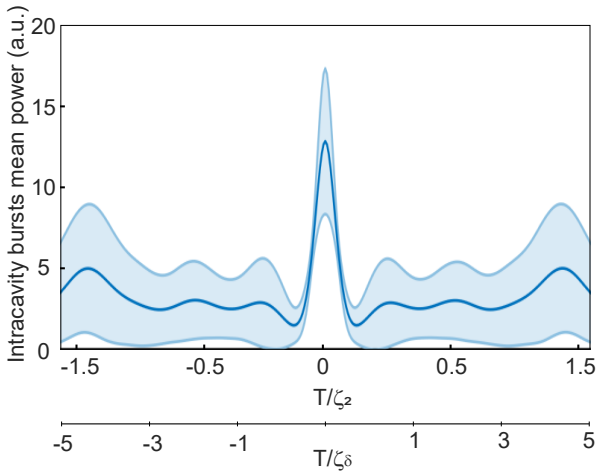


**Figure 5:** Mean profile of the intensity bursts with the standard deviation range (shaded region) in the unit of  $\xi_\delta$  and  $\xi_2 = \xi_l$  for  $\Delta = 1.1$  and  $S = 4.9$ .

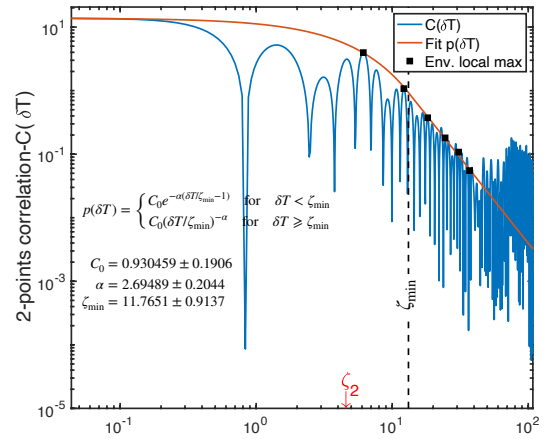


**Figure 6:** Equal time two-points correlation function in logarithmic scale. The red line correspond to the fit of the envelop with the function  $p(\delta T)$  in inset. Black squares to the local maxima of the envelop.

law as proposed in [38, 39]. We have analysed our data of  $C(\delta T)$  according to this proposition. The result is given in Fig. 6. As expected, this figure shows a region where the envelope of  $C(\delta T)$  follows a power law, which is initially preceded by a region where the distribution is exponential. The starting point of this power law is three times larger than the exponential decay range. In addition, the exponential decay range obtained following the reference [39], is about 4.88. This is of the same order than the values we have previously obtained by detecting the trend two-points correlation function. Hence, in our analysis, the exponential regime allows us to determine the size of subdomains for the forecasting.

#### 5.4. Prediction horizon

There are many definitions of the prediction time of chaotic evolution. These definitions converge to the same value when dealing with low dimensional chaos with a few positive Lyapunov exponents. The widely used is the Lyapunov time given  $T_{\lambda_m} = 1/\max(\lambda_i)$ . However, this time has some limitations for high-dimensional systems. In that

	$\Delta T_p$ [ps]				
	22	45	180	360	
$(S/S_{th})^2$	11	3.66	1.83	0.47	0.23
	14	2.85	1.32	0.34	0.16
	20	1.81	0.81	0.21	0.10
	23	1.31	0.71	0.18	0.09

Table 1: Lifetime of spatiotemporal chaotic fluctuations in fraction of the cavity roundtrip.  $\Delta T_p$  is the duration of the pump temporal window and  $(S/S_{th})^2$  is the ratio between the pump power  $S^2$  and the threshold value  $S_{th}^2$ .

case, the maximal local Lyapunov exponent can be a good alternative. So far the bursts are the most chaotic objects in the system. We can follow the local Lyapunov exponent together with the local evolution as shown in Fig. 7. We can see that the local values of the maximum Lyapunov exponent correspond to the emergence of at least one burst and are much larger than the mean value  $\lambda_m = 0.8$  (see

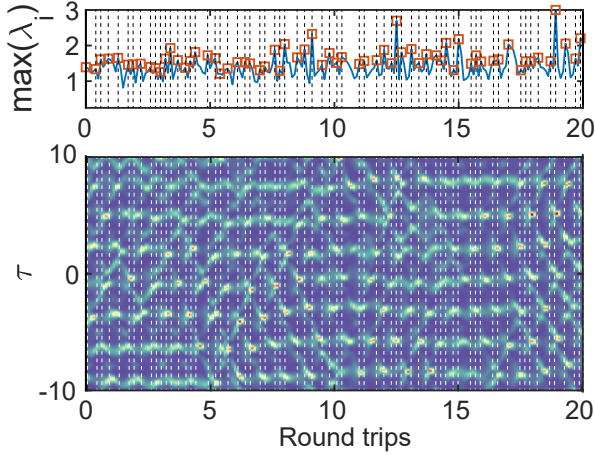


**Figure 7:** Maximal local Lyapunov exponent (top panel) and the corresponding roundtrip evolution (bottom panel). Red square mark the local maxima of the largest Lyapunov exponents. Vertical lines give the local of the largest burst over the roundtrips.

Fig. 3(c)). The Lyapunov time given by the mean value of these local features is  $T_{\lambda_i} \simeq 3$  roundtrips. This time scale has to be compared with the Kolmogorov-Sinai entropy time [40, 41]. This entropy is estimated as  $h_{KS} = \sum \lambda_m$  with  $\lambda_m$  the positive Lyapunov exponents. Then  $T_{KS} = 1/h_{KS}$  gives the time scale of entropy production by the system. We have computed this time for different pump temporal windows and pump intensities. This is summarized in Table 1. In our configuration this time is smaller than a roundtrip time. Consequently, our prediction horizons are larger than the characteristic time of the chaos in the system.

## 6. Precursors-driven machine learning

Since the spatiotemporal chaos generated in the resonator is highly dimensional, ( $\Delta T_{stc} \ll \Delta T_p$  and  $\tau_{stc} < t_R$ ), forecasting the fully developed turbulence of the fiber ring cavity is a great challenge. Recent use of neural networks has opened new perspectives in this field [9, 42–45]. In particular, in [9, 42], the authors have used an echo state network to reproduce the dynamics of the Kuramoto-Shivashinsky equation over several Lyapunov times. It also shows that increasing the size of the system requires larger network nodes with the same forecasting accuracy. This would be almost impossible in our system presenting a much higher spatiotemporal chaotic behavior compared to these works. Here, we propose to investigate an alternative to the forecast of the complete field under study. It consists of identifying a precursor of an event of interest and extracting a subdomain around it to reduce the complexity of the forecasting and increase the accuracy of the predictions. For this purpose, we compute the information flow to optimize the determination of the size of subdomains. The transfer entropy 2D map is presented in Fig. 8(b) (numerics) and Fig. 8(g) (experiments). At finite roundtrips, it exhibits either a central peak ( $P0_i$ ) or double peak ( $P1_i$ ) structures. As an example,

the temporal profiles of roundtrip lags  $P0_1$  and  $P1_1$ , the most powerful, are shown in Fig. 8(a) and (f). Experimental traces are temporally wider because of the finite band-pass of the detection system with a noise background inherent to experiments, but a pretty good agreement with numerics is obtained. These peaks mean that, on average, any peaks in the evolution carry information from its own past. This information vanishes roundtrip to roundtrip (Fig. 8(b) and 8(g)), the amplitude of the peaks following an exponential decay as can be seen in Fig. 8(c) and 8(h). The dual peaks structure of the  $P1_i$  has the advantage to be easily differentiated compared to the single peak of the  $P0_i$  making  $P1_i$  the better choice than bursts precursors. Furthermore, the time shift between the peaks of the  $P1_i$  is of the same order of the equal time correlation range  $\xi_2$  (see Appendix C). It can be appropriated to be the order of magnitude of our subdomains. Each measurement is locally centered at the location of the intensity burst. Given that information converges from  $P1_j$  towards  $P0_i$  we can make an association  $\{P0_i, P1_j\} (|T - T_k| \leq \xi_2)$  and perform a supervised machine learning training, with  $T_k$  being the location of the  $k$ -th local peak.

The network in Fig. 1 is a deep Long Short-Term Memory (LSTM) encoder-decoder algorithm which has been shown to be suitable for sequence-to-sequence forecasting [46, 47]. We used two sets of data: either two simulation runs or two experimental campaigns of recordings. One for training and testing, and the other one to evaluate fully independently the forecasting accuracy of our system. Figures 8(d) and 8(e) show the highly forecasting correlation skill on the test data for two roundtrip lags,  $P1_1$ ,  $P1_2$ , from numerics, and figures 8(i) and 8(j) from experiments. The correlation is close to 97% for  $P1_1$  and only decays to 60% for  $P1_2$  in numerics proving the excellent performance of our method. In experiments (Figs. 8(i) and 8(j)), while data are noisy, correlation factors remain still close to 1, with 75% and 64% for  $P1_1$  and  $P1_2$ , respectively.

After training and testing are completed, we can now follow the evolution looking for the precursors. For the detection, we have used a moving window convolution of the current roundtrip with the profile of the  $P1_i$ . Once a double peak precursors identified in the running roundtrip we feed of our multi-level network, and then we predict the positions of pulses that will appear  $m$  roundtrips later. We performed the same process for numerical simulations and experiments. The positions of reconstructed local predictions (*when* and *where*) are presented in circles in Figs. 9(a) and (b), superimposed on spatiotemporal traces of the output cavity. As illustrated on the right-hand side of Fig. 9(b), precursors are identified at roundtrip  $n$  to forecast pulses which will appear at roundtrip  $n + 9$ . This is 3 times the horizon given by the local maximum Lyapunov exponent. We obtained a better accuracy in the predictions for numerical simulations (Fig. 9(a)) because experimental data (Fig. 9(b)) are noisier. The shape of the predicted pulses ("*what is coming ?*") is also predicted from our algorithm. Typical examples are depicted in Figs. 9(c) to 9(e). An

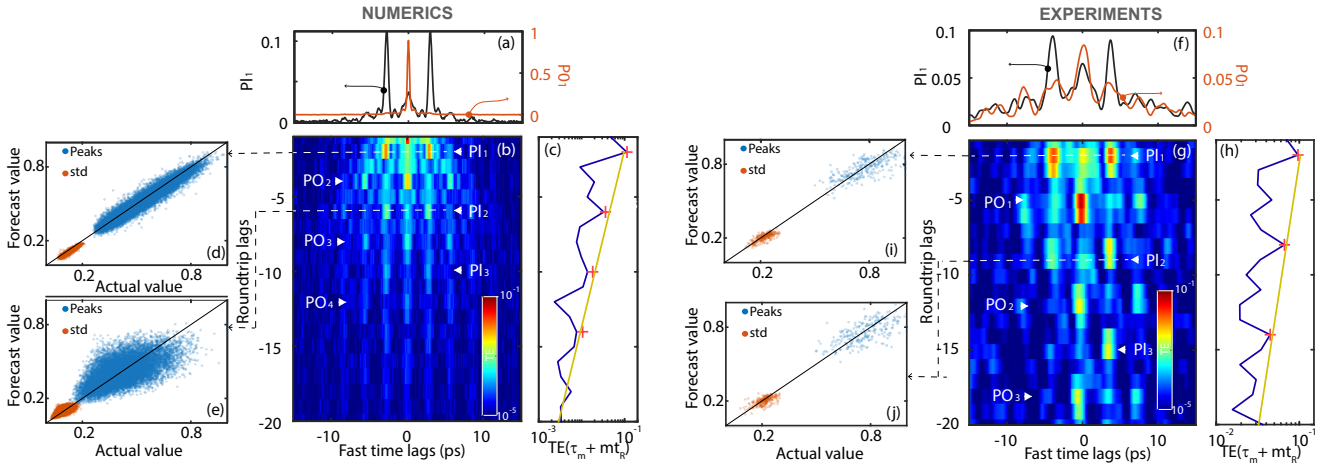


**Figure 8:** (a)-(e) Numerical simulations of the LLE (Eq. (2) in Appendix A) and (f)-(j) from experiments in a Kerr resonator. (b) and (g) show the 2D plot of the transfer entropy. (a) and (f) represent profiles of  $P_{01}$  and  $P_{11}$ . The evolution of the transfer entropy at the fast time lag given by the  $P_{11}$  maximum with respect to the roundtrip lags are shown in (c) and (h). The blue solid line shows the evolution of the transfer entropy as a function of the roundtrips, the symbols (+) mark peaks at each  $P_{1n}$ , and the straight yellow line the best exponential fit from these maxima. (d) and (e) show correlation maps after the supervised training using the association between detected pulses and their  $P_{11}$  and  $P_{12}$  precursors respectively from numerical simulations and (i) and (j) from experiments. In panels (d), (e), (i), and (j) the horizontal axes, *Actual value*, stands for the measured peak value (blue points) and the standard deviation of the observed pulses (red points). The vertical axes, *Forecast value*, accounts for the predicted peak value and their standard deviation.

	$P_{11}$	$P_{12}$	$P_{13}$
False-positive precursors (%)	6.66	8	14.92
True-positive precursors (%)	74.60	71.30	66.4
Pulses without precursors (%)	25.40	28.70	33.6
Prediction accuracy (%)	96.60	60	-
Roundtrip forecast	3	9	15

Table 2: Performances of the method as a function of the double peaks precursor ( $P_{1i}$ )

excellent agreement is achieved compared to the reference traces. The performances of the predictions in terms of false-positive and accuracy are summarized in Table 2. For  $P_{13}$ , predictions at  $n + 9$  roundtrips is possible with less than 8% of false-positive precursors while operating in a strongly chaotic spatiotemporal regime. At this horizon, the accuracy is about 60%. By slightly lowering the pump power from 3.3 to 3 times the cavity threshold ( $P_{12}$ ), the regime is still strongly chaotic. While we get the same ratio of false-positive prediction, we reach 75% of prediction accuracy at  $n+6$  roundtrips. For weakly spatiotemporal chaotic regimes, between two and three times the cavity threshold, the prediction are almost perfect.

This value is remarkable for such a high-dimensional chaotic system. We also point out that all predictions based on  $P_{11}$  reach an accuracy above 90% without any deep optimization of the network. The LSTM encoder-decoder are not the unique recurrent neural network that could perform the forecasting process. However, the main purpose of our work was to show that precursors can be used to make a model-free

prediction of extreme events in a high-dimensional chaotic system.

## 7. Conclusion

We have shown that forecasting high-dimensional chaos is possible by splitting the system around the objects of interest. We identify these objects by mapping the transfer entropy. This quantity is also used to estimate the extension range of the subsystem, the precursors of the object of interest, and also the forecasting horizon of the dynamics. By detecting the precursors, we can therefore build a triggerable model-free process in which the "when?" and "where?" are no more the concerns but the "what is coming?". The level of the transfer entropy affects only the accuracy of this prediction. Our analysis was based on the Long Short-Term Memory encoder-decoder algorithm. However, other methods can be implemented to recognize precursor-pulse pairs, such as gate recurrent unit, echo state network, and deep learning. The optimal recognition method of precursor-pulse pairs is an open problem. Our protocol can be applied to any nonlinear systems independently from its size provided that information flows are correctly computed.

## Acknowledgements

SC, AM, FB acknowledge the LABEX CEMPI (ANR-11-LABX-0007) as well as the Ministry of Higher Education and Research, Hauts de France council and European Regional Development Fund (ERDF) through the Contract de Projets Etat-Region (CPER Photonics for Society P4S), the French government through the Programme Investissement



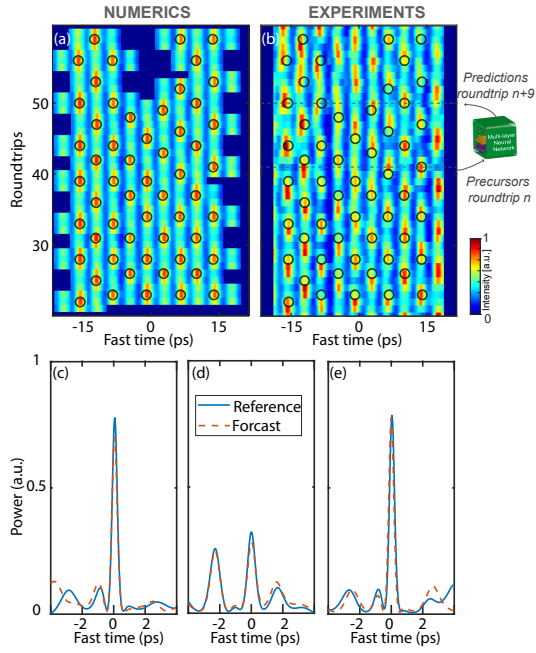


**Figure 9:** Predictions of the *when* and *where* in circles,  $n+9$  round-trips after a precursor is detected, superimposed on the spatiotemporal evolution of the field at the cavity output, (a) from numerics and (b) experiments. (c)-(e) Examples of the *what is coming?* prediction: forecast pulse in orange dashed lines (predicted shape) to be compared to the reference one in blue solid lines. More comparison are provided as an additional material (plot\_pred\_anim.gif). The normalised parameters are  $\Delta = 1.1$  and  $S = 5.0$ . Accuracy metrics give that 92% of the P1<sub>1</sub> precursors produce true positive prediction.

d’avenir (I-SITE ULNE/ANR-16-IDEX-0004 ULNE), the CNRS (IRP LAFONI project) Equipex T-REFIMEVE and H2020 Marie Skłodowska-Curie Actions (MSCA)(713694). M.G.C. thanks for the financial support of FONDECYT project 1210353 and Millennium Institute for Research in Optics, ANID–Millennium Science Initiative Program-ICN17\_012.

## Author contributions

A.M. and F.B. conceived, designed and performed the experiments. Numerical simulations based on the LLE were carried out by S.C. and M.G.C. The development of analytical tools and characterization of the ST chaos was performed by S.C. and M.G.C.. All authors participated in the analysis and interpretation of the results and the writing of the paper.

## A. Numerical simulations

In the experimental setup, the propagation of light in an optical fiber loop is modeled without loss of generality by the nonlinear Schrödinger equation augmented with boundary conditions or Ikeda map [24, 29, 48]:

$$\partial_z A(z, T) = -i\frac{\beta_2}{2}\partial_T^2 A(z, T) + i\gamma A(z, T)|A(z, T)|^2$$

$$A(0, T + T_R) = \sqrt{\theta}E_i(T) + \sqrt{\rho}A(L, T)e^{-i\Phi_0},$$

where  $T_R$  stands for the round-trip time, which is the time taken by the pulse to propagate along the cavity with the group velocity,  $\Phi_0$  is the linear phase shift,  $\theta$  ( $\rho$ ) is the mirror transmission (reflection) coefficient, and  $L$  is the cavity length. The complex amplitude of the electric field inside the cavity is  $A$ . Each of the coefficients  $\beta_2$  is responsible for the second-order dispersion, and  $\gamma$  is the nonlinear coefficient of the fiber. The independent variable  $z$  refers to the longitudinal coordinate, while  $T$  is the time in a reference frame moving with the group velocity of the light. For large enough cavity finesse  $\mathcal{F} = \pi/\alpha$ , with  $\alpha$  the effective losses of the cavity, the evolution of the electric field inside the loop is well described by the Lugiato-Lefever equation [29, 30]:

$$\frac{\partial\psi}{\partial t} = S - (1 + i\Delta)\psi - i\eta\frac{\partial^2\psi}{\partial\tau^2} + i|\psi|^2\psi, \quad (2)$$

where  $S = 2E_i\sqrt{\gamma L/\alpha^3}$ ,  $\psi = A\sqrt{\gamma L/\alpha}$ ,  $t = \alpha T/T_R = \alpha m$ , and  $\tau = T/T_n$  with  $T_n = \sqrt{|\beta_2 L|/(2\alpha)}$ .  $\delta = (2k\pi - \Phi_0)/\alpha$  is the detuning with respect to the nearest cavity resonance  $k$ . The integer  $m$  gives the roundtrip number and the coefficient  $\eta = \pm 1$  is the sign of the group velocity dispersion term. The configuration of our setup gives  $\alpha = 0.20$ ,  $\Delta = 1.1$  and  $T_n \simeq 1.1$  ps.

## B. Lyapunov spectrum computation

Strictly speaking, to prove a spatiotemporal chaotic dynamics, one may compute several quantities. In particular, it is mandatory to compute the Lyapunov spectrum. Next, this spectrum must have a positive part and continuous region whose area has to linearly increase with the size of the system. The computation of the Lyapunov spectrum itself is very well documented [14] and is not the purpose here. Let just recall the main steps. From the state of the system at a given time, the linear evolution of any small perturbation  $\delta\mathbf{X}$  can be described by  $\partial_t\delta\mathbf{X} = \mathbf{J}\delta\mathbf{X}$ , where  $\mathbf{J}$  is the respective Jacobian. In the present case, we introduce  $\psi = \psi_r + i\psi_i$ , with  $\psi_r$  and  $\psi_i$  being the real and imaginary part of  $\psi$  respectively. At a time  $t = t_0$ , introducing  $\psi = \psi_0 + \delta\psi$ , with  $\delta\psi \ll \psi(t = t_0) = \psi_0$  the matrix  $\mathbf{J}$  reads :

$$\mathbf{J} = \begin{bmatrix} -(1 + 2\psi_{0r}\psi_{0i}) & \Delta - \psi_{0r}^2 - 3\psi_{0i}^2 - \partial_\tau^2 \\ -\Delta + (\psi_{0i}^2 + 3\psi_{0r}^2) + \partial_\tau^2 & -(1 - 2\psi_{0r}\psi_{0i}) \end{bmatrix}, \quad (3)$$

and  $\delta\mathbf{X} = (\delta\psi_r, \delta\psi_r)^t$ . Suppose that we want to compute the  $n$ -th first dominant exponents of the spectrum, we introduce the matrix  $\mathbf{L}$ , that contains  $n$  orthonormal vectors  $\mathbf{v}_i$  which to be used as initial conditions when solving  $\partial_t\delta\mathbf{X} = \mathbf{J}\delta\mathbf{X}$ :

$$\mathbf{L}(t = t_0) \equiv [\mathbf{v}_1 \quad \mathbf{v}_2 \quad \dots \quad \mathbf{v}_n] = \begin{bmatrix} x_{11} & x_{12} & x_{13} & \dots & x_{1n} \\ x_{21} & x_{22} & x_{23} & \dots & x_{2n} \\ \dots & \dots & \dots & \dots & \dots \\ x_{d1} & x_{d2} & x_{d3} & \dots & x_{dn} \end{bmatrix},$$

(4)

where  $d$  is the dimension of the system. After a time increment  $dt$ , the matrix  $\mathbf{L}$  evolves to  $\mathbf{L}(t_0 + dt) = \hat{\mathbf{U}}\mathbf{L}(t_0)$  where  $\hat{\mathbf{U}} = e^{\mathbf{J}^*dt}$ . Using the modified Gram-Schmidt QR decomposition on  $\mathbf{L}(t_0 + dt)$ , the diagonal elements of  $\mathbf{R}$  account for the Lyapunov exponents  $\tilde{\lambda}_i$  ( $i = 1, \dots, n$ ) at time  $t_0 + dt$ , that is

$$\tilde{\lambda}_i(t_0 + dt) = \frac{1}{dt} \ln(\mathbf{R}_{ii}(t_0 + dt)). \quad (5)$$

Repeating this procedure several time, after a large number of iterations  $N$ , the Lyapunov exponents can be approximated by

$$\lambda_i \equiv \langle \tilde{\lambda}_i \rangle = \frac{1}{Ndt} \sum_{k=1}^N \ln(\mathbf{R}_{ii}(t_0 + kdt)). \quad (6)$$

From the spectrum  $\{\lambda_i\}$  an estimator of the dimension of the chaotic attractor is given by the Kaplan-Yorke dimension  $D_{KY} = p + \sum_{i=1}^p \lambda_i / |\lambda_{p+1}|$  where  $p$  is such that  $\sum_{i=1}^p \lambda_i > 0$  and  $\sum_{i=1}^{p+1} \lambda_i < 0$  [12]. For a one-dimensional system of size  $L$ , a spatiotemporal chaos implies that  $D_{KY}$  increase linearly with  $L$ .

### C. Determination of the subdomains to forecast

In a spatiotemporal chaotic system many quantities can be used as order parameter. Considering the extensive feature of this chaos, the Kaplan-Yorke dimension may change linearly with the volume of the system [3, 35]. Namely, for a 1D system,  $D_{YK} = \xi_\delta^{-1} \Delta T$  where  $\Delta T$  is the extension of the system and  $\xi_\delta$  represents the dimension correlation length of the system for a fixed value of the control parameter. This is an intensive quantity which gives an estimation of the extension of the dynamically independent subsystems. Together with the dimension correlation length one can compute the correlation length  $\xi_2$ . This length is defined as the exponential decay range of the equal time two-point correlation [33–35]:

$$C(\Delta\tau) = \langle (\psi(\Delta\tau + \tau', t) - \langle \psi \rangle) (\psi(\tau', t) - \langle \psi \rangle) \rangle, \quad (7)$$

where the brackets  $\langle \cdot \rangle$  stand for the average process. The direct determination of  $C(\Delta\tau)$  is quite costly in calculation time. However, by using the Wiener-Khintchin theorem [37, 49], it is computed by the following process: first time-averaging the Fourier spectra and next taking the inverse Fourier transform of its magnitude squared. Since the experimental spectra result from an averaging process over a large number of cavity roundtrip,  $C(\Delta\tau)$  can also be computed taking the inverse Fourier transform of the measured spectrum. Hence, for the LL equation (2), we have computed  $\xi_\delta$  and  $\xi_2$  with respect to the input pump intensity. The third length we have computed is the long range decay rate of the transfer entropy  $\xi_{TE}$ . The region around the burst to forecast is largest range between  $\xi_\delta$ ,  $\xi_2$  and  $\xi_{TE}$ . Detailed implementation can be found in the SI.

Model:

Layer (type)	Output Shape	Param #
lstm_1 (LSTM)	(None, 3, 820)	3365280
lstm_2 (LSTM)	(None, 820)	5382480
repeat_vector (RepeatVector)	(None, 1, 820)	0
lstm_3 (LSTM)	(None, 1, 820)	5382480
lstm_4 (LSTM)	(None, 1, 820)	5382480
time_distributed_10 (TimeDistr)	(None, 1, 205)	168305
Total params: 19,681,025		
Trainable params: 19,681,025		
Non-trainable params: 0		

Table 3: Python LSTM encoder-decoder summary for the network we have trained with linear activation function. We have used the package Tensorflow-Keras. For the optimization we have used the following options: "optimizer=Adam(), loss='Huber', metrics='mae'".

### D. The forecasting protocol

Protocol of the forecasting process

**From data:**

- Compute the transfer entropy map
- Detect the pulses
- Move backward to the chosen history

**The training:**

- compute the PDF from peaks amplitude
- split data 80% for training and 20% for testing with the same PDFs
- Standardize input data (precursors) : Yeo-Johnson transform
- Create the LSTM encoder-decoder (see Table 3)

**Forecasting:**

- Watch the dynamics for precursors
- If precursor detected feed the network to forecast the incoming pulse at the chosen horizon and location

### References

- [1] Henri Poincaré. *Science et méthode*. Ernest Flammarion, 2014.
- [2] Edward N. Lorenz. Deterministic nonperiodic flow. *J. Atmos. Science*, 20(2):130 – 141, 01 Mar. 1963. doi: 10.1175/1520-0469(1963)020<0130:DNF>2.0.CO;2.
- [3] David Ruelle. Large volume limit of the distribution of characteristic exponents in turbulence. *Commun. Math. Phys.*, 87(2):287–302, 1982.
- [4] T Li and JA Yorke. Period three implies chaos the american mathematical monthly. 1975.
- [5] MC Cross and PC Hohenberg. Spatiotemporal chaos. *Science*, 263(5153):1569–1569, 1994.
- [6] Goëry Genty, Lauri Salmela, John M. Dudley, Daniel Brunner, Alexey Kokhanovskiy, Sergei Kobtsev, and Sergei K. Turitsyn. Machine

- learning and applications in ultrafast photonics. *Nature Photonics*, 15(2):91–101, February 2021. ISSN 1749-4893. doi: 10.1038/s41566-020-00716-4. URL <https://www.nature.com/articles/s41566-020-00716-4>. Number: 2 Publisher: Nature Publishing Group.
- [7] Hamed Ghoddsi, Germán G Creamer, and Nima Rafizadeh. Machine learning in energy economics and finance: A review. *Energy Economics*, 81:709–727, 2019.
- [8] Cynthia Rudin, David Waltz, Roger N Anderson, Albert Boulanger, Ansaf Salleb-Aouissi, Maggie Chow, Haimonti Dutta, Philip N Gross, Bert Huang, Steve Jerome, et al. Machine learning for the new york city power grid. *IEEE transactions on pattern analysis and machine intelligence*, 34(2):328–345, 2011.
- [9] Pantelis R Vlachas, Wonmin Byeon, Zhong Y Wan, Themistoklis P Sapsis, and Petros Koumoutsakos. Data-driven forecasting of high-dimensional chaotic systems with long short-term memory networks. *Proceedings of the Royal Society A: Mathematical, Physical and Engineering Sciences*, 474(2213):20170844, 2018.
- [10] Yoo-Geun Ham, Jeong-Hwan Kim, and Jing-Jia Luo. Deep learning for multi-year enso forecasts. *Nature*, 573(7775):568–572, 2019.
- [11] Xiaofeng Li, Bin Liu, Gang Zheng, Yibin Ren, Shuangshang Zhang, Yingjie Liu, Le Gao, Yuhai Liu, Bin Zhang, and Fan Wang. Deep-learning-based information mining from ocean remote-sensing imagery. *National Science Review*, 7(10):1584–1605, 2020.
- [12] Edward Ott. *Chaos in dynamical systems*. Cambridge university press, 2002.
- [13] Alan Wolf, Jack B Swift, Harry L Swinney, and John A Vastano. Determining lyapunov exponents from a time series. *Physica D: nonlinear phenomena*, 16(3):285–317, 1985.
- [14] Ch Skokos. The lyapunov characteristic exponents and their computation. In *Dynamics of Small Solar System Bodies and Exoplanets*, pages 63–135. Springer, 2010.
- [15] David Cai, David W McLaughlin, and Jalal Shatah. Spatiotemporal chaos in spatially extended systems. *Mathematics and computers in simulation*, 55(4-6):329–340, 2001.
- [16] Claude Elwood Shannon. *The Mathematical Theory of Communication by CE Shannon and W. Weaver*. 1949.
- [17] Thomas Schreiber. Measuring information transfer. *Phys. Rev. Lett.*, 85:461–464, Jul 2000. doi: 10.1103/PhysRevLett.85.461.
- [18] Joseph T. Lizier, Mikhail Prokopenko, and Albert Y. Zomaya. Local information transfer as a spatiotemporal filter for complex systems. *Phys. Rev. E*, 77:026110, Feb 2008. doi: 10.1103/PhysRevE.77.026110. URL <https://link.aps.org/doi/10.1103/PhysRevE.77.026110>.
- [19] Michael Wibral, Nicolae Pampu, Viola Priesemann, Felix Siebenhühner, Hannes Seiwert, Michael Lindner, Joseph T Lizier, and Raul Vicente. Measuring information-transfer delays. *PLoS one*, 8(2):e55809, 2013.
- [20] Fatimah Abdul Razak and Henrik Jeldtoft Jensen. Quantifying causality in complex systems: understanding transfer entropy. *PLoS One*, 9(6):e99462, 2014.
- [21] Patrick Boba, Dominik Bollmann, Daniel Schoepe, Nora Wester, Jan Wiesel, and Kay Hamacher. Efficient computation and statistical assessment of transfer entropy. *Frontiers in Physics*, 3:10, 2015.
- [22] Joseph T. Lizier. Jidt: An information-theoretic toolkit for studying the dynamics of complex systems. *Frontiers in Robotics and AI*, 1: 11, 2014. ISSN 2296-9144. doi: 10.3389/frobt.2014.00011. URL <https://www.frontiersin.org/article/10.3389/frobt.2014.00011>.
- [23] Florent Bessin, François Copie, Matteo Conforti, Alexandre Kudlinski, Arnaud Mussot, and Stefano Trillo. Real-time characterization of period-doubling dynamics in uniform and dispersion oscillating fiber ring cavities. *Phys. Rev. X*, 9:041030, Nov 2019. doi: 10.1103/PhysRevX.9.041030. URL <https://link.aps.org/doi/10.1103/PhysRevX.9.041030>.
- [24] Stéphane Coen and Marc Haelterman. Modulational instability induced by cavity boundary conditions in a normally dispersive optical fiber. *Phys. Rev. Lett.*, 79(21):4139, 1997.
- [25] Stéphane Coen, Marc Haelterman, Philippe Emplit, Laurent Delage, Lotfy Mokhtar Simohamed, and François Reynaud. Bistable switching induced by modulational instability in a normally dispersive all-fibre ring cavity. *Journal of Optics B: Quantum and Semiclassical Optics*, 1(1):36, 1999.
- [26] Reza Salem, Mark A Foster, and Alexander L Gaeta. Application of space–time duality to ultrahigh-speed optical signal processing. *Advances in Optics and Photonics*, 5(3):274–317, 2013.
- [27] Saliya Coulibaly, Majid Taki, Abdelkrim Bendahmane, Guy Millot, Bertrand Kibler, and Marcel Gabriel Clerc. Turbulence-induced rogue waves in kerr resonators. *Phys. Rev. X*, 9(1):011054, 2019.
- [28] Alessia Pasquazi, Marco Peccianti, Luca Razzari, David J Moss, Stéphane Coen, Miro Erkintalo, Yanne K Chembo, Tobias Hansson, Stefan Wabnitz, Pascal Del’OHaye, et al. Micro-combs: A novel generation of optical sources. *Physics Reports*, 729:1–81, January 2018. ISSN 0370-1573. doi: 10.1016/j.physrep.2017.08.004. URL <http://www.sciencedirect.com/science/article/pii/S0370157317303253>.
- [29] Marc Haelterman, Stefano Trillo, and Stefan Wabnitz. Dissipative modulation instability in a nonlinear dispersive ring cavity. *Optics communications*, 91(5-6):401–407, 1992.
- [30] Luigi A Lugiato and René Lefever. Spatial dissipative structures in passive optical systems. *Phys. Rev. Lett.*, 58(21):2209, 1987.
- [31] Mozheng Wei. Quantifying local instability and predictability of chaotic dynamical systems by means of local metric entropy. *International Journal of Bifurcation and Chaos*, 10(01):135–154, 2000.
- [32] Robert Shaw. Strange attractors, chaotic behavior, and information flow. *Zeitschrift für Naturforschung A*, 36(1):80–112, 1981.
- [33] Corey S O’hern, David A Egolf, and Henry S Greenside. Lyapunov spectral analysis of a nonequilibrium ising-like transition. *Phys. Rev. E*, 53(4):3374, 1996.
- [34] David A Egolf and Henry S Greenside. Relation between fractal dimension and spatial correlation length for extensive chaos. *Nature*, 369(6476):129–131, 1994.
- [35] Mark C Cross and Pierre C Hohenberg. Pattern formation outside of equilibrium. *Rev. Mod. Phys.*, 65(3):851, 1993.
- [36] Reif Frederick. *Fundamentals of statistical and thermal physics*. 1965.
- [37] David A Egolf and Henry S Greenside. Characterization of the transition from defect to phase turbulence. *Phys. Rev. Lett.*, 74(10): 1751, 1995.
- [38] Anna D Broido and Aaron Clauset. Scale-free networks are rare. *Nature communications*, 10(1):1–10, 2019.
- [39] Aaron Clauset, Cosma Rohilla Shalizi, and Mark EJ Newman. Power-law distributions in empirical data. *SIAM review*, 51(4):661–703, 2009.
- [40] Ch. Dellago and H. A. Posch. Mixing, lyapunov instability, and the approach to equilibrium in a hard-sphere gas. *Phys. Rev. E*, 55: R9–R12, Jan 1997. doi: 10.1103/PhysRevE.55.R9. URL <https://link.aps.org/doi/10.1103/PhysRevE.55.R9>.
- [41] A. Gualandi, J.-P. Avouac, S. Michel, and D. Faranda. The predictable chaos of slow earthquakes. *Science Advances*, 6(27), 2020. doi: 10.1126/sciadv.aaz5548. URL <https://advances.sciencemag.org/content/6/27/eaaz5548>.
- [42] Jaideep Pathak, Brian Hunt, Michelle Girvan, Zhixun Lu, and Edward Ott. Model-free prediction of large spatiotemporally chaotic systems from data: A reservoir computing approach. *Phys. Rev. Lett.*, 120: 024102, Jan 2018. doi: 10.1103/PhysRevLett.120.024102.
- [43] Pablo Amil, Miguel C Soriano, and Cristina Masoller. Machine learning algorithms for predicting the amplitude of chaotic laser pulses. *Chaos: An Interdisciplinary Journal of Nonlinear Science*, 29(11):113111, 2019.
- [44] Mushegh Rafayelyan, Jonathan Dong, Yongqi Tan, Florent Krzakala, and Sylvain Gigan. Large-scale optical reservoir computing for spatiotemporal chaotic systems prediction. *Physical Review X*, 10(4): 041037, 2020.
- [45] Junjie Jiang and Ying-Cheng Lai. Model-free prediction of spatiotemporal dynamical systems with recurrent neural networks: Role of network spectral radius. *Physical Review Research*, 1(3):033056, 2019.

- [46] Sepp Hochreiter and Jürgen Schmidhuber. Long short-term memory. *Neural Computation*, 9(8):1735–1780, 1997. doi: 10.1162/neco.1997.9.8.1735.
- [47] Yann LeCun, Yoshua Bengio, and Geoffrey Hinton. Deep learning. *nature*, 521(7553):436–444, 2015.
- [48] Kensuke Ikeda. Multiple-valued stationary state and its instability of the transmitted light by a ring cavity system. *Optics communications*, 30(2):257–261, 1979.
- [49] Frederick Reif. *Fundamentals of statistical and thermal physics*. Waveland Press, 2009.